ACS APPLIED ENERGY MATERIALS

www.acsaem.org Article

Electrospun Composite Gel Polymer Electrolytes with High Thermal Conductivity toward Wide Temperature Lithium Metal Batteries

Huihui Gan,[‖] Jiale Yuan,[‖] Yong Zhang, Shaoqiao Li, Liping Yu, Jirong Wang, Ji Hu,* Nuo Yang,* and Zhigang Xue*

Cite This: *ACS Appl. Energy Mater.* 2021, 4, 8130–8141 Read Online

ACCESS | Metrics & More | Article Recommendations | Supporting Information

ABSTRACT: Herein, the thermally conductive composite polymer membranes (CPMs) with silica-coated silver nanowires (AgNWs@SiO_2) and poly(vinylidene fluoride-hexafluoropropylene) (PVDF-HFP) are first fabricated by an electrospinning technique. Various composite gel polymer electrolytes (CGPEs) are investigated with different weight percentages of AgNWs@SiO_2 with respect to PVDF-HFP in the presence of liquid electrolytes. The CPMs display high thermal conductivity and thermal stability, good mechanical strength, and high electrolyte uptake. The thermal conduction property of CPMs was analyzed by a bidirectional asymmetric heat transfer model. Moreover, the CGPEs with the electrospun CPM as the matrix and AgNWs@SiO_2 as fillers (es-CGPEs) possess the high ionic conductivity and excellent electrochemical performance compared to the Celgard separator system. The Li/es-CGPEs/$LiFePO_4$ cell shows an enlarged excellent cycling life and better rate performance at 25 and 60 °C, in comparison to the one without AgNWs@SiO_2 fillers. Interestingly, the Li/es-CGPEs/$LiFePO_4$ cell in the presence of 5 wt % of AgNWs@SiO_2 still delivers an excellent rate capability at 0 °C. The es-CGPE with AgNWs@SiO_2 would be a promising candidate as the electrolyte material toward wide temperature lithium metal batteries.

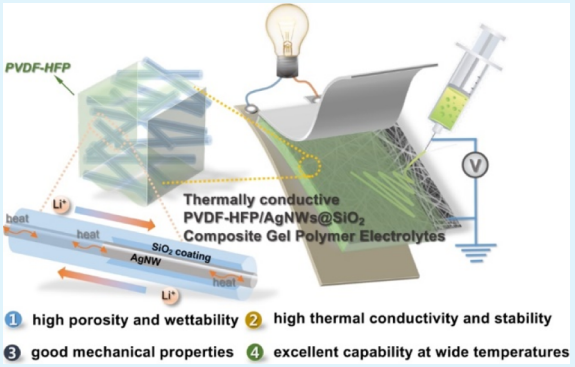

KEYWORDS: *thermal conduction, AgNWs@SiO_2, electrospinning technique, composite polymer membranes, lithium metal batteries*

INTRODUCTION

Lithium-ion batteries (LIBs) have been considered as promising power sources for power portable electronic devices such as mobile phones, watches, laptops, digital cameras, and other electric vehicles.[1−8] Currently, higher energy density of next-generation lithium metal batteries (LMBs) has attracted considerable attention due to high theoretical capacity (3860 mA h g^{-1}) and very low redox potential (−3.04 V vs standard hydrogen electrode) of the lithium metal anode.[9−17] However, the large volume change of the lithium metal and the growth of lithium dendrites[18−21] during the cycling process leads to serious safety hazards, such as internal short circuit, flammability, and explosion,[22−26] further hindering their practical application in LMBs.

To overcome the abovementioned issues, tremendous strategies have widely been applied to suppress Li dendrite growth, including the fabrication of an artificial solid electrolyte interface layer,[27,28] electrolyte additives,[29,30] functional separator,[31,32] and polymer electrolytes (PEs).[33,34] Generally, PEs can be divided into gel PEs (GPEs) and solid PEs . Recently, GPEs have intensively attracted attention because of their high ionic conductivity and good interfacial contact with the electrode.[35] Poly(vinylidene fluoride-hexafluoropropylene) (PVDF -HFP),[36] poly(vinylidene fluoride) (PVDF),[37] poly(acrylonitrile),[38] polyethylene terephthalate,[39] poly(ether ketone),[40] poly(methyl methacrylate),[41] and poly(ethylene oxide)[42] are the host polymers that are most widely used for preparing GPEs. Among them, PVDF-HFP is one of the most commonly polymer matrices for GPEs due to its high dielectric constant, outstanding mechanical strength, good affinity with liquid electrolytes, and excellent thermal/electrochemical stability.[43,44] To further improve the mechanical strength and ionic conductivity of GPEs, inorganic fillers such as $Li_{6.4}Ga_{0.2}La_3Zr_2O_{12}$, SiO_2, Al_2O_3, $MgAl_2O_4$, ZnO, TiO_2, and mesoporous zeolite have been incorporated into the polymer matrix to form composite gel PEs (CGPEs).[44−49]

As mentioned above, the prepared CGPEs could exhibit good electrochemical performance in batteries. Nevertheless, inorganic fillers are usually difficult to be well dispersed in the polymer matrix, resulting in the worsened thermal and mechanical properties of composite materials. It is worth

Received: May 18, 2021
Accepted: July 21, 2021
Published: July 31, 2021

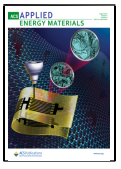

https://doi.org/10.1021/acsaem.1c01420
ACS Appl. Energy Mater. 2021, 4, 8130–8141

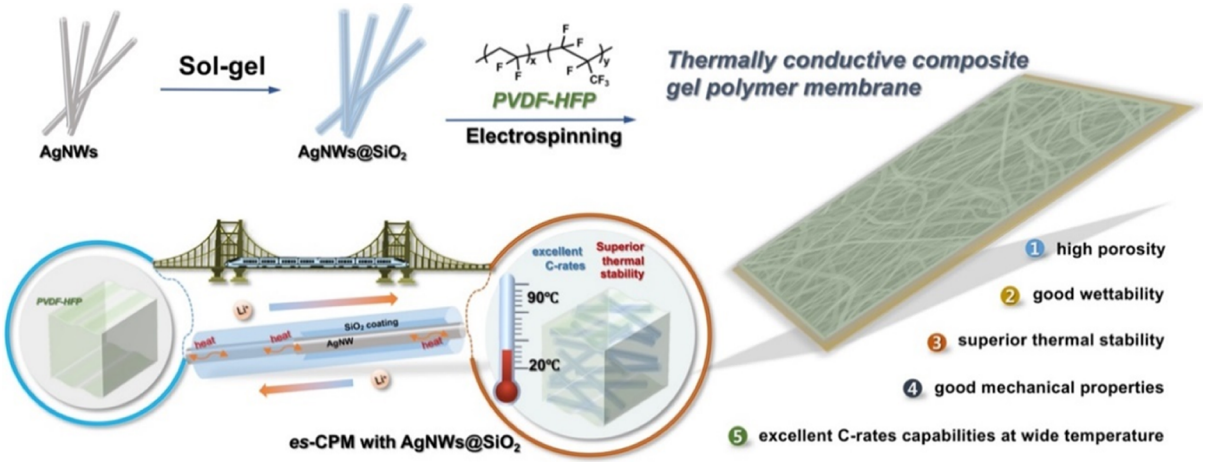

Figure 1. Schematic illustration of the PVDF-HFP/AgNWs@SiO_2 es-CGPEs.

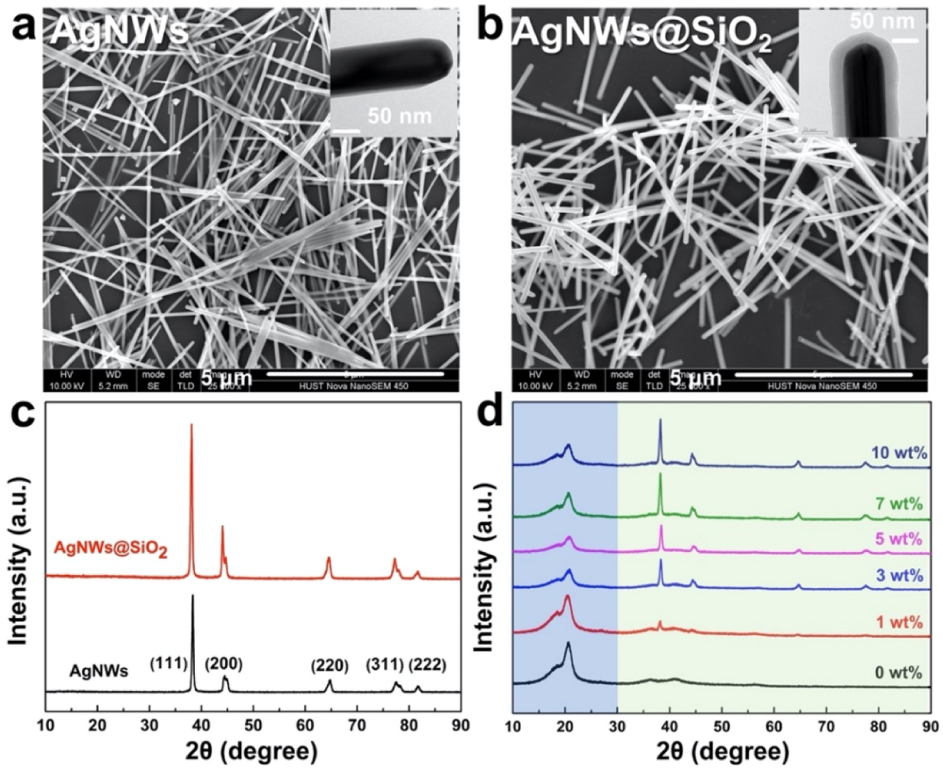

Figure 2. (a) SEM image of AgNWs. The inset is a TEM image of AgNWs. (b) SEM image of AgNWs@SiO_2. The inset is a TEM image of AgNWs@SiO_2. (c) XRD patterns of AgNWs and AgNWs@SiO_2. (d) XRD patterns of PVDF-HFP/AgNWs@SiO_2 es-CPMs with various loadings of AgNWs@SiO_2.

noting that the mixture of polymer matrix and inorganic fillers being used as an electrospinning solution to extensively fabricate composite polymer membranes (CPMs) is an effective method to improve the dispersion of nanofillers and enhance the comprehensive performances of electrospun CGPEs (es-CGPEs). Meanwhile, a wide operating temperature range should be satisfied in practical applications for lithium batteries. It is well known that the high temperature significantly reduces cycle life and may trigger thermal runaway. However, only a few works focus on the research of thermal management inside batteries.[50−52] Enhancing thermal conduction inside batteries can promote heat dissipation and decrease the temperature inhomogeneity and the thermal stress in batteries. Therefore, it is necessary to develop a high thermal conductivity of PEs for batteries. In our previous works, we have reported the high-performance thermally conductive composites for the application in the electronic packaging.[53−55] It can be found that silver nanowires (AgNWs) exhibit intrinsic high thermal and electrical conductivities. However, AgNWs are mostly difficult to be well dispersed in the polymer matrix. Consequently, one-dimensional core−shell structural silica-coated AgNWs (AgNWs@SiO_2) could be considered as the ideal inorganic fillers for CPMs. AgNWs@SiO_2 not only can facilitate the heat dissipation in es-CGPEs but also can be well dispersed in the polymer matrix and avoid the occurrence of short circuit during the cycling of batteries at elevated temperature. In short, the prepared es-CGPEs can exhibit high thermal

https://doi.org/10.1021/acsaem.1c01420
ACS Appl. Energy Mater. 2021, 4, 8130−8141

conductivity and thermal stability, good mechanical strength, and superior electrochemical performance in LMBs.

Herein, the thermally conductive PVDF-HFP/AgNWs@SiO_2 es-CGPEs with one-dimensional AgNWs@SiO_2 as inorganic fillers were fabricated by the electrospinning technology to significantly enhance the mechanical and thermal properties, thermal conductivity, and electrochemical performances (Figure 1). The AgNWs@SiO_2 can exhibit continuous ion pathways owing to the generation of uniform permeability networks rather than through lots of particle−particle junctions. Meanwhile, the incorporation of AgNWs@SiO_2 could reduce the polymer crystallinity. In this study, the prepared CPMs display superior thermal stability and thermal conductivity, high porosity, and sufficient electrolyte wettability. The high-performance LMBs with the good cycling life and excellent rate capability were also assembled with PVDF-HFP/AgNWs@SiO_2 es-CGPEs.

EXPERIMENTAL SECTION

Materials. Sodium chloride (NaCl, 99.5%, Aladdin), silver nitrate ($AgNO_3$, 99.8%, Aladdin), ethylene glycol (EG, 99.0%, Aladdin), tetraethyl orthosilicate (TEOS, 99.99%, Aladdin), poly(vinylpyrrolidone) (PVP, M_w = 40,000, Sigma-Aldrich), acetone (99.5%, Sinopharm Chemical Reagent Co., Ltd.), *N*,*N*-dimethylformamide (DMF, 99.9%, Aladdin), ethanol (99.7%, Sinopharm Chemical Reagent Co., Ltd.), ammonium hydroxide (NH_4OH, 25−28%, Aladdin), PVDF microfiltration membrane (3 μm pore size, Shanghai Xingya Purification Material Factory), PVDF-HFP (M_w = 455,000, Aldrich), and 1.0 M of lithium hexafluorophosphate ($LiPF_6$) in ethylene carbonate (EC)/ethyl methyl carbonate (EMC)/diethyl carbonate (DEC) (1:1:1, v/v/v, DoDoChem) were used as received. Lithium iron phosphate ($LiFePO_4$, LFP), acetylene black (AB), and *N*-methyl-2-pyrrolidone were purchased locally and used as received.

Synthesis of AgNWs. The AgNWs were synthesized according to our previous works with some modifications.[53−55] PVP (M_w = 40,000, 4.01 g) was dissolved in 75.85 g of EG with moderate stirring and heated to 167 °C. Then, 120 μL of NaCl solution (0.2 M) was added. After 1 min, 40 μL of $AgNO_3$ solution (1 M) was added. Then, after 5 min, 2.4 mL of $AgNO_3$ solution (1 M) was added at the rate of 0.6 mL min^{-1} by a peristaltic pump. When the reaction solution began to turn greyish-green from transparent, all residual $AgNO_3$ solution was added at the rate of 5.2 mL min^{-1}. The system was then stirred for 30 min and cooled to room temperature. The AgNW suspension was diluted with ethanol (300 mL) and filtered through a PVDF membrane. The purification process was repeated three times to remove the EG and excess PVP. The scanning electron microscopy (SEM) images and X-ray diffraction (XRD) patterns of AgNWs are shown in Figure 2.

Synthesis of AgNWs@SiO_2. SiO_2-coated AgNWs (AgNWs@SiO_2) with a core−shell nanostructure were synthesized as follows. 1 g of AgNWs was added into an ethanol/NH_4OH/deionized water (100:2.8:20, v/v/v) solution under mechanical stirring. Then, 2.1 mL of TEOS solution (7 vol % of TEOS in ethanol) was added dropwise to the mixture. The obtained mixture was further stirred about 24 h at room temperature. Finally, AgNWs@SiO_2 was collected by vacuum filtering. The SEM images and XRD patterns of AgNWs@SiO_2 are shown in Figure 2.

Preparation of PVDF-HFP/AgNWs@SiO_2 CPMs. To fabricate the PVDF-HFP/AgNWs@SiO_2 CPMs, six samples were dispersed with a different weight ratio of AgNWs@SiO_2 (0, 1, 3, 5, 7, and 10 wt %) with respect to PVDF-HFP in solvents DMF and acetone (3:7, w/w). The concentrations of AgNWs@SiO_2 and PVDF-HFP were both 12 wt %. Then, the solution was placed into a 10 mL of syringe with a stainless-steel needle. Electrospinning was performed by applying a voltage of 13 kV. After electrospinning, the electrospun CPMs (es-CPMs) were dried at 80 °C in a vacuum oven in order to remove the residual solvent. The thickness (T) of the es-CPMs is 60 ± 20 μm. A schematic illustration of the electrospinning process and SEM images of es-CPMs are shown in Figures 1 and 3, respectively.

Characterization. XRD (X'Pert, PRO PANalytical BV, Netherlands) was used for phase identification using Cu Kα radiation (40 mA/40 kV). The morphology of the sample was characterized by SEM and high-resolution transmission electron microscopy (TEM). The composition was measured by energy-dispersive X-ray spectroscopy (EDAX Octane SU, USA). The Fourier transformation infrared (FT-IR) absorption spectra were applied on an FT interferometer (Equinox 55, Bruker, Germany). The thermal stability was examined through a thermogravimetric analyzer (TGA, 4000 PerkinElmer, USA) under N_2 with a heating rate of 10 °C min^{-1} from 30 to 800 °C. Differential scanning calorimetry (DSC) was used on a differential scanning calorimeter (Q2000, TA, USA) at a heating rate of 10 °C min^{-1} under N_2. The es-CPMs were evaluated by adsorption and desorption of N_2 by a Brunauer−Emmett−Teller surface area measurement system (ASAP2420-4MP, USA). The pore area and pore size of es-CPM were measured by a mercury porosimeter (MicroActive AutoPore V 9600 Version, USA). The wettability of the es-CPMs with liquid electrolytes was examined using an optical contact angle measuring and contour analysis systems (OCA20). The stress−strain of the es-CPMs was measured through an electronic universal testing machine at the rate of 10 mm min^{-1} (CMT4104, Shenzhen San Testing Machine Co.).

The liquid electrolyte uptake of the es-CPMs was measured in the following way. First, the dried es-CPMs (the weight of the dry es-CPMs, m_0) were immersed in the liquid electrolyte [1.0 M $LiPF_6$ in EC/EMC/DEC (1:1:1, v/v/v)] overnight in an Ar-filled glovebox at room temperature to form es-CGPEs. Then, the es-CGPEs were taken out of the liquid electrolyte and gently wiped with a filter paper until the weight of the es-CGPEs (the weight of the liquid absorbed es-CGPEs, m_1) did not change. The absorbability ratio (η) was calculated as follows

$$\eta = (m_1/m_0 - 1) \times 100\%$$

The porosity (P) of the es-CPMs was measured by gravimetry. The dried es-CPMs were weighed and then soaked in 1-butanol for 24 h. The wet es-CPMs were weighted again by gently wiping with the filter paper. The porosity (P) can be calculated as follows

$$P = [(m_B - m_M)/\rho_B]/[(m_B - m_M)/\rho_B + m_M/\rho_M]$$

where m_M and m_B are the mass of the dry and wet es-CPMs, respectively, and ρ_B and ρ_M are the densities of 1-butanol and the es-CPMs, respectively.

The thermal conductivity (κ) of es-CPMs was measured by the 3ω method,[56] which was widely used in the κ measurement of thin film materials.[57] As an electrothermal frequency-domain measurement, the Joule heating was calculated by the 3ω method and the electrical signals were detected via temperature rise. In brief, the heater is driven by an alternating current at frequency ω. The Joule heating causes the temperature oscillation at frequency 2ω, and so does the resistance of the heater. The oscillating current and resistance generate a voltage signal at frequency 3ω, which can be detected by measurement platform.

Electrochemical Measurements. The ionic conductivity (σ) of the es-CGPEs was measured by electrochemical impedance spectroscopy (EIS) analysis in the frequency range of 1 MHz to 10 Hz at a temperature range from 30 to 100 °C using an electrochemical workstation (Autolab PGSTAT302N, Netherlands). The es-CGPEs were sandwiched between two stainless steel (SS) electrodes to form the SS/es-CGPEs/SS symmetrical cell. The bulk electrolyte resistance (R_b) of the es-CGPEs referring to ionic conductance was measured by an EIS method, and the ionic conductivity was calculated by the equation

$$\sigma = L/(R_b S)$$

where S is the area of the es-CGPEs, and L is the thickness of the es-CGPEs.

https://doi.org/10.1021/acsaem.1c01420
ACS Appl. Energy Mater. 2021, 4, 8130−8141

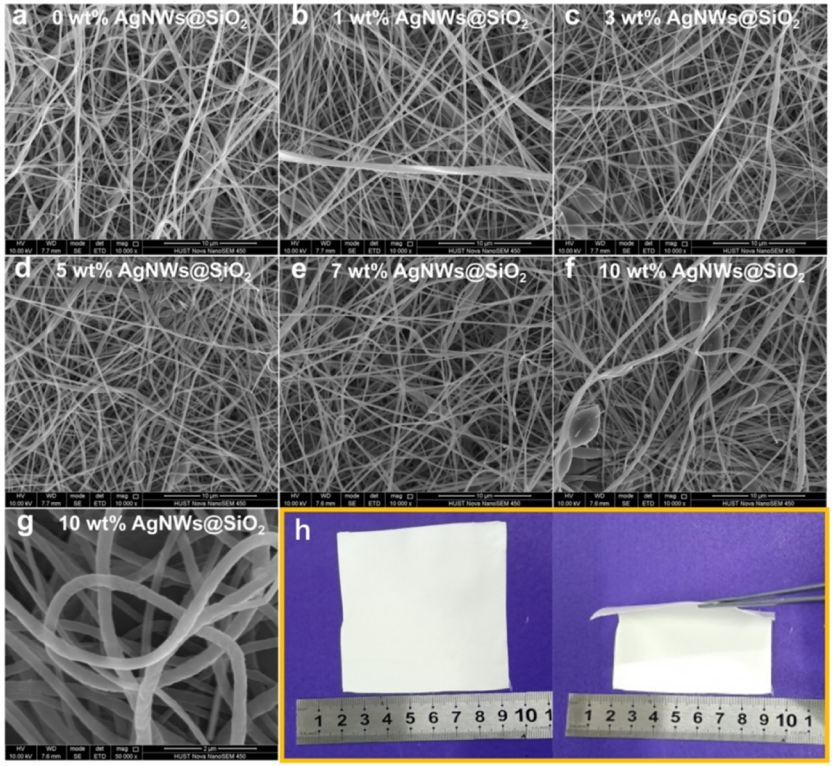

Figure 3. SEM images of PVDF-HFP/AgNWs@SiO_2 es-CPMs with (a) 0, (b) 1, (c) 3, (d) 5, (e) 7, and (f,g) 10 wt % of AgNWs@SiO_2. Scale bar is 10 μm for (a–f) and 2 μm for (g). (h) Optical image of es-CPM with 5 wt % of AgNWs@SiO_2.

The electrochemical stability window was evaluated by linear sweep voltammetry (LSV) from 0 to 6 V at a scan rate of 1 mV s^{-1} at 60 °C. The es-CGPEs were sandwiched between lithium foil and an SS electrode in an asymmetrical cell.

The interfacial stability between es-CGPEs and lithium foil was evaluated by a Li/es-CGPEs/Li symmetric cell at 60 °C. The symmetric cells were under constant current density of 0.5 mA cm^{-2}. The symmetric cells were charged for 1 h and discharged for 1 h during each cycle.

The cathode was prepared by mixing LFP, AB, and PVDF in a mass ratio of 8:1:1. The slurry was coated on the surface of an aluminum foil current collector and dried at 80 °C for 24 h in a vacuum oven. The loading and thickness of LFP cathode were 1.5 ± 0.5 mg cm^{-2} and 15 ± 5 μm, respectively. The charge–discharge cycle tests were investigated by fabricating a CR2032 coin cell composed of LFP cathode, lithium foil, and es-CGPEs or Celgard separator with the liquid electrolyte [~60 μL, 1.0 M $LiPF_6$ in EC/EMC/DEC (1:1:1, v/v/v)].

RESULTS AND DISCUSSION

Physical Structure and Characterizations. Figures 2a,b shows the morphologies and sizes of AgNWs and AgNWs@SiO_2 by SEM and TEM. The diameter and length of AgNWs are 50–150 nm and 5–15 μm, respectively. The AgNWs@SiO_2 with the core–shell nanostructure was obtained by uniformly coating about 40 nm thick SiO_2 on the surface of the AgNWs. Figure 2c exhibits the XRD patterns for the AgNWs and AgNWs@SiO_2. The diffraction peaks in the XRD of AgNWs can be indexed to a face-centered cubic phase of Ag (JCPDS no. 04-0783). Five diffraction peaks at 38.4, 44.5, 64.7, 77.4, and 81.8° agree with the (111), (200), (220), (311), and (222).[58] Meanwhile, no SiO_2 phases are detected, which indicates that the diffraction peak of the SiO_2 thin layer is an amorphous structure or the signals of the SiO_2 layer are overwhelmed by the strong diffraction peak of Ag. Therefore, five peaks of AgNWs are still observed in the XRD pattern of AgNWs@SiO_2. Figure 2d shows two diffraction peaks at 18.5 and 20.2°, which agree with the (100) and (020) crystalline phases of the PVDF-HFP membrane.[59] The characteristic diffraction peaks of AgNWs@SiO_2 at 38.4, 44.5, 64.7, 77.4, and 81.8° appear in the XRD patterns of PVDF-HFP/AgNWs@SiO_2 es-CPMs with various loadings of AgNWs@SiO_2. Not only the intensity of PVDF-HFP diffraction peak at 20.2° in PVDF-HFP/AgNWs@SiO_2 es-CPMs is decreasing but also the crystallinity (X_c) is reducing (Table S1). These results indicate that the crystallinity of PVDF-HFP could be decreased by the addition of AgNWs@SiO_2 inorganic fillers.

Figure 3 shows the SEM images of PVDF-HFP/AgNWs@SiO_2 es-CPMs with various loadings of AgNWs@SiO_2 fillers. The highly porous membranes with three-dimensional network structures were obtained from the electrospinning technique, and the es-CPMs exhibits good flexibility. The highly porous structure in composite fiber membranes can absorb more liquid electrolytes, and the crystalline phase of the pure PVDF-HFP matrix can also be reduced with the addition of AgNWs@SiO_2 fillers, which will enhance the ionic conductivity of es-CGPEs. The fiber diameter distribution of es-CPMs is shown in Figure S1, the fiber diameter of es-CPMs will be increased with the addition of AgNWs@SiO_2, and most of the fiber diameter was distributed in the range of 100–500 nm. For the es-CPM with 5 wt % of AgNWs@SiO_2, the fiber diameter distribution was between 200 and 350 nm. The surface area and pore size of es-CPM were studied by N_2 adsorption/desorption isotherms measurements. As shown in Figure S2, the specific surface areas of es-CPM were 6.00 ± 1.00 m^2 g^{-1} and the pore size distribution of es-CPM was mainly around from 2 to 20 nm. In addition, the pore area and pore size distribution of es-CPMs with 0 and 5 wt % of AgNWs@SiO_2

https://doi.org/10.1021/acsaem.1c01420
ACS Appl. Energy Mater. 2021, 4, 8130–8141

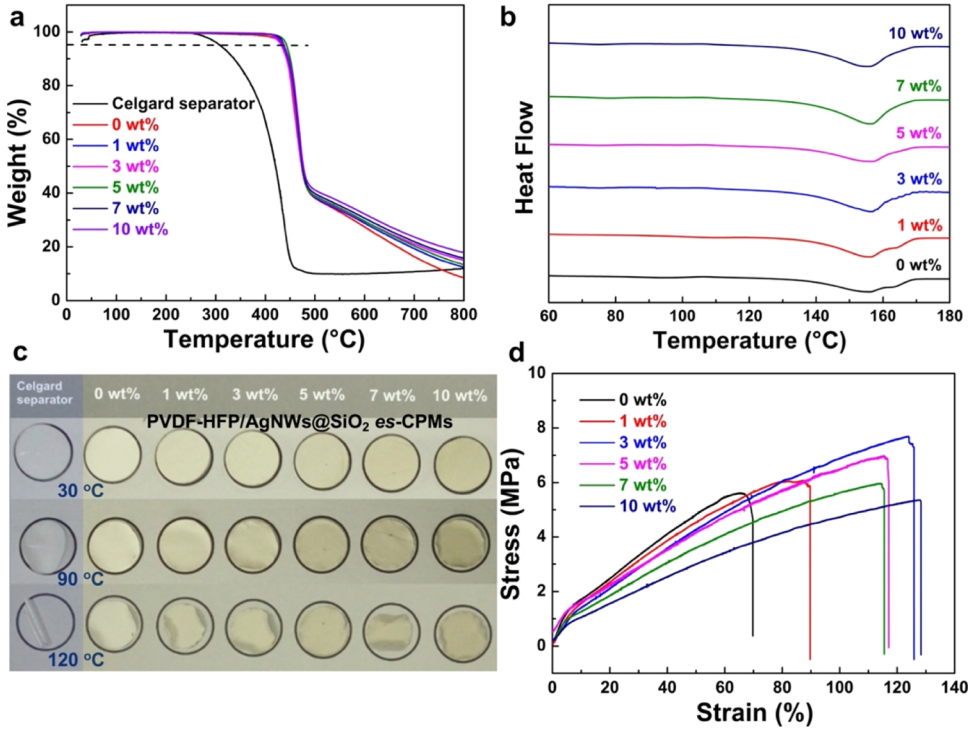

Figure 4. (a) TGA curves of the Celgard separator and PVDF-HFP/AgNWs@SiO_2 es-CPMs. (b) DSC curves of PVDF-HFP/AgNWs@SiO_2 es-CPMs. (c) Thermal shrinkage of the Celgard separator and PVDF-HFP/AgNWs@SiO_2 es-CPMs at different temperatures for 12 h. (d) Stress−strain curves of PVDF-HFP/AgNWs@SiO_2 es-CPMs.

were accurately measured by a mercury porosimeter (Figure S3). The average pore diameter of es-CPMs with 0 and 5 wt % of AgNWs@SiO_2 were 1840 and 1420 nm, respectively. Figure S4 shows the FT-IR spectra of AgNWs@SiO_2 es-CPMs. The characteristic absorption peak at 1402 cm^{-1} is due to the stretching vibration of C−F, which is the characteristic peak of the PVDF-HFP copolymer. The characteristic absorption peak at 1181 cm^{-1} is assigned to the C−C bond of PVDF. In all es-CPMs, the characteristic absorption peak of AgNWs@SiO_2 is suppressed by PVDF-HFP, and no evident shift in peaks was observed in composite fiber membranes, indicating that there are no new chemical bonds formed between PVDF-HFP and AgNWs@SiO_2.

Thermal Properties. The thermal ability of the PEs plays a key role in influencing the safety and electrochemical performance for LMBs. Figure 4a shows the TGA curves of the Celgard separator and PVDF-HFP/AgNWs@SiO_2 es-CPMs with various loadings of AgNWs@SiO_2 fillers. It is shown that the decomposition temperature ($T_{d,5\%}$) of the Celgard separator is around 376 °C. The corresponding $T_{d,5\%}$ value of all es-CPMs is above 435 °C, which is much higher than that of the Celgard separator. When the temperature reaches 500 °C, 30 wt % of es-CPMs remains after degradation. Furthermore, the remaining weights of es-CPMs are still more than the pure PVDF-HFP membrane and the Celgard separator as the temperature is up to 700 °C, demonstrating the excellent thermal stability of composite fiber membranes. These results may be mainly attributed to the following reasons. On the one hand, the AgNWs@SiO_2 is still maintained when the temperature is up to 500 °C. On the other hand, the passivation layer will be formed with the addition of AgNWs@SiO_2, which is beneficial to the heat transport and serves as an insulator for mass during thermal degradation. DSC curves of es-CPMs are presented in Figure 4b. It is observed that the melting temperature of es-CPMs (Table S1) is about 156 °C, which exhibits the characteristic peaks of pristine PVDF-HFP. All these results indicate that the superior thermal stability of es-CPMs is able to meet the practical requirement of LMBs and is much safer than the Celgard separator. Figure 4c shows the thermal shrinkage behaviors at different temperatures for 12 h. The PVDF-HFP/AgNWs@SiO_2 es-CPMs exhibit better dimensional stability at a high temperature (90 or 120 °C) than that of the commercial Celgard separator owing to the excellent thermal stability of es-CPMs.

Mechanical Performances. The mechanical properties of the es-CPMs during the packaging and cycling processes are especially important for their applications in LMBs. Figure 4d and Table S1 show the stress−strain curves of the es-CPMs with various loadings of AgNWs@SiO_2. The cross-linked network formed via the electrospun nanofibers endows the es-CPMs with good dimensional stability, and the incorporation of AgNWs@SiO_2 fillers can improve the mechanical strength. Compared with the electrospun PVDF-HFP membrane, mechanical properties of es-CPMs are importantly improved in the presence of a lower concentration of AgNWs@SiO_2. The es-CPM with 3 wt % of AgNWs@SiO_2 fillers possesses 7.7 MPa of stress and 126% of elongation at break. With the increase of AgNWs@SiO_2 loading, the tensile strength of es-CPMs shows a decreasing tendency. AgNWs@SiO_2 tends to be agglomerated and is poorly dispersed in es-CPM fibers with a high filler loading. However, the elongation at break of es-CPMs is higher than that of the electrospun PVDF-HFP membrane. The es-CPMs with good flexibility and high toughness are more suitable for application in LMBs. The AgNWs@SiO_2 nanofillers with a large surface area and small

https://doi.org/10.1021/acsaem.1c01420
ACS Appl. Energy Mater. 2021, 4, 8130−8141

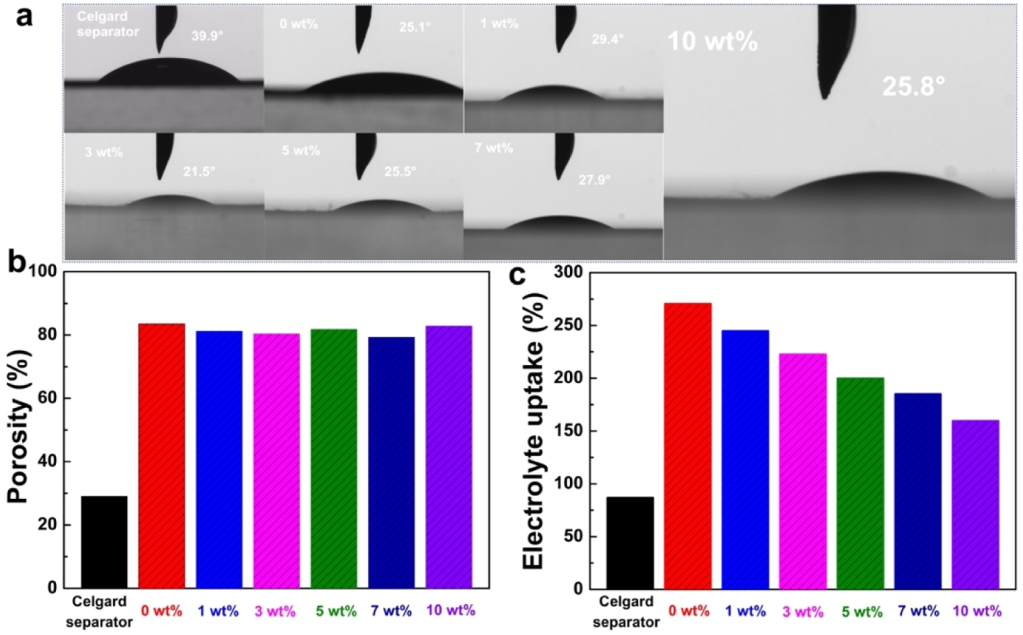

Figure 5. (a) Contact angle photographs, (b) porosity, and (c) electrolyte uptake of the Celgard separator and PVDF-HFP/AgNWs@SiO_2 es-CPMs.

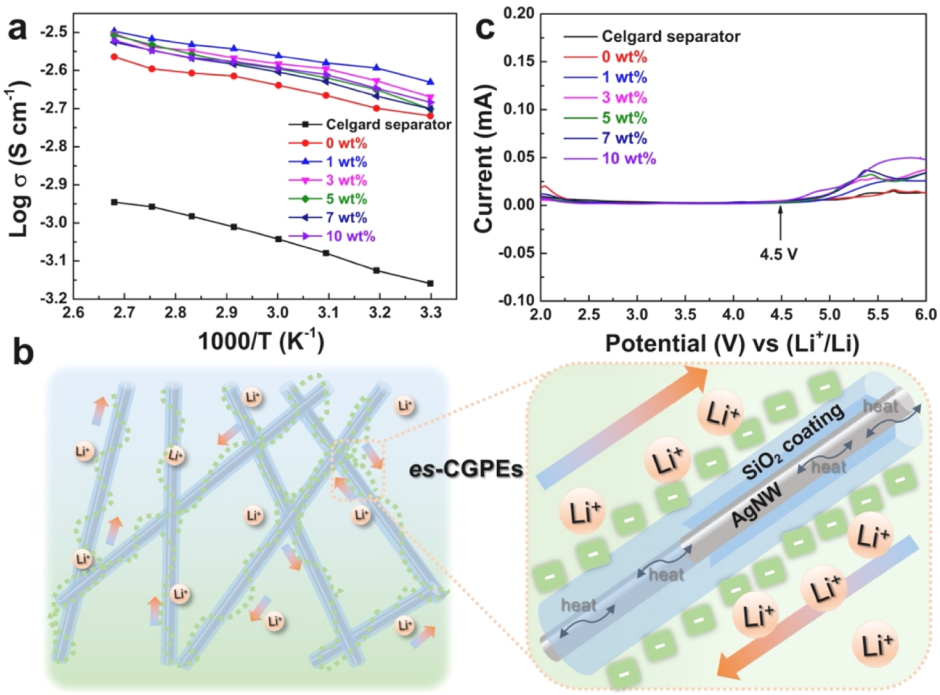

Figure 6. (a) Ionic conductivities of the Celgard separator and PVDF-HFP/AgNWs@SiO_2 es-CGPEs. (b) Proposed ion pathways in es-CGPEs. (c) LSV at a scan rate of 1 mV s^{-1} at 60 °C.

size possess a large contact area with the electrospun PVDF-HFP fibers. The microcracking formed in the stretching process of es-CPMs has the ability to absorb the impact energy. Overall, the es-CPMs provide good control over the stretchability while maintaining high mechanical strength.

Contact Angle, Porosity, and Electrolyte Uptake. The wetting behavior of the PEs also plays a key factor for electrochemical performance, and the PEs should be easily wetted by the liquid electrolyte. Figure 5a shows that the contact angle of PVDF-HFP/AgNWs@SiO_2 es-CPMs is lower than that of the Celgard separator. The lower contact angle indicates that es-CPMs are more easily wetted by a liquid electrolyte, which is beneficial to enhancing the liquid absorbability of the PEs. Moreover, an optimal porosity is beneficial to trapping sufficient electrolytes within the pores of the PEs to maintain good ionic conductivity. Figures 5b,c shows that the PVDF-HFP/AgNWs@SiO_2 es-CPMs have higher porosities (about 80%) and absorb more liquid electrolytes than the Celgard separator owing to the porous three-dimensional network structures. The electrolyte uptake of the electrospun PVDF-HFP membrane is up to around 270%, and the uptake of es-CPMs is higher than that of the

https://doi.org/10.1021/acsaem.1c01420
ACS Appl. Energy Mater. 2021, 4, 8130−8141

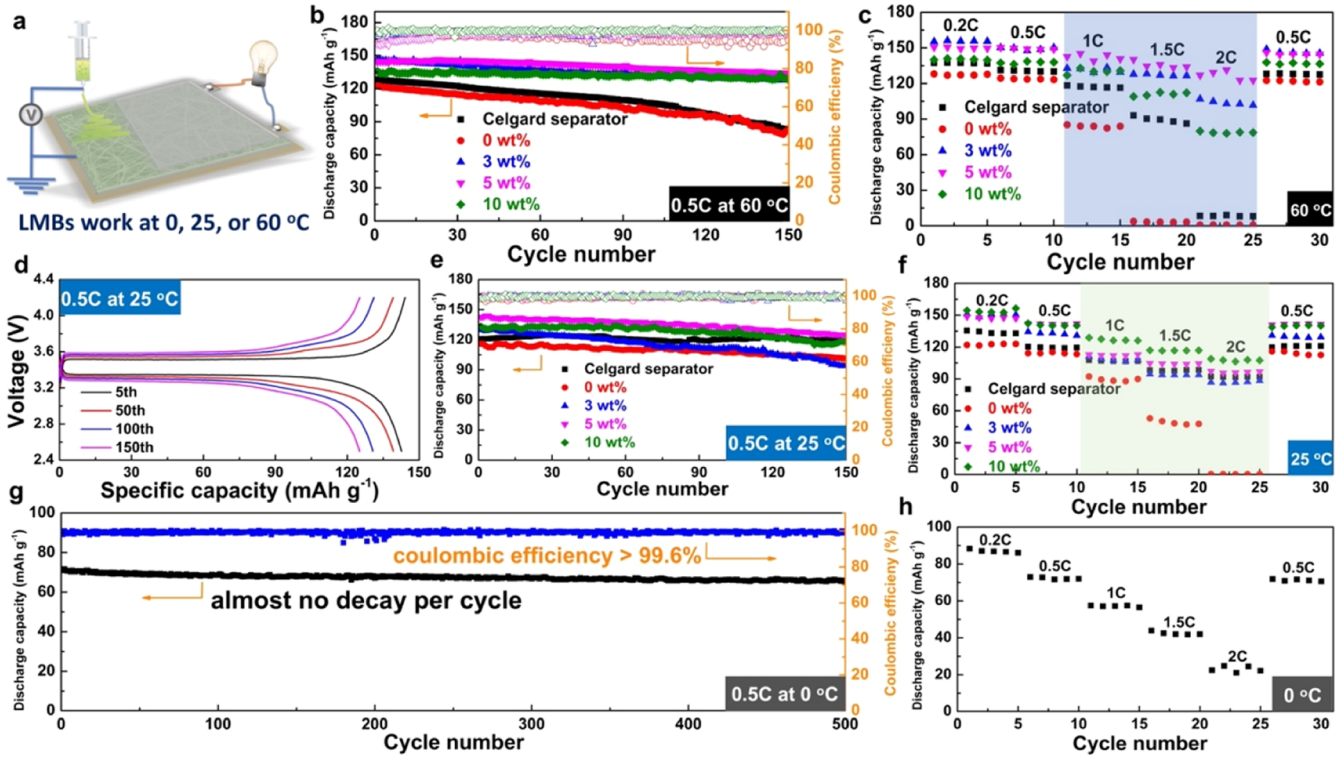

Figure 7. (a) Schematic illustration of LMBs assembled with various separators. (b) Cycling performance of Li/es-CGPEs/LFP cells operated at 0.5 C at 60 °C. (c) Rate performance of cells at 60 °C at different rates of 0.2, 0.5, 1, 1.5, and 2 C. (d) Charge−discharge curves of Li/es-CGPEs/LFP cells with different cycles at 0.5 C at 25 °C in the case of 5 wt % of AgNWs@SiO_2. (e) Cycling performance of Li/es-CGPEs/LFP cells operated at 0.5 C at 25 °C. (f) Rate performance of the Li/es-CGPEs/LFP cells at 25 °C at different rates of 0.2, 0.5, 1, 1.5, and 2 C. (g) Cycling performance at 0.5 C at 0 °C. (h) Rate performance of Li/es-CGPEs/LFP cells at 0 °C at different rates of 0.2, 0.5, 1, 1.5, and 2 C.

Celgard separator (87%), resulting from the high porosity of es-CPMs. The electrospun fibers and the interconnected pore structure make the es-CPMs much easier to absorb the liquid electrolytes. Importantly, the PVDF-HFP matrix in es-CPMs can also exhibit a good affinity with the liquid electrolytes. Although the electrolyte uptake of es-CPMs decreases because of the addition of high loading of AgNWs@SiO_2, the uptake of es-CPM with 10 wt % of AgNWs@SiO_2 is still as high as 160%. All the performances show that the es-CPMs fabricated in this work pose a huge potential to enhance the ion transmission ability, which could lead to the practical application of high-performance LMBs.

Electrochemical Performances. Figure 6a exhibits the ionic conductivity for all the membranes over the temperature from 30 to 100 °C. It is observed that CGPEs (es-CGPEs) formed via the introduction of liquid electrolytes into es-CPMs display clearly higher ionic conductivity than the Celgard separator (0.69×10^{-3} S cm^{-1} at 30 °C). The ionic conductivities of es-CGPEs with 0, 1, 3, 5, 7, and 10 wt % of AgNWs@SiO_2 at 30 °C are 1.91×10^{-3}, 2.34×10^{-3}, 2.14×10^{-3}, 1.99×10^{-3}, 1.99×10^{-3}, and 2.07×10^{-3} S cm^{-1}, respectively. The porous three-dimensional network structures and high porosity endow the AgNWs@SiO_2/PVDF-HFP es-CGPEs with improved ionic conductivity. Interestingly, compared with the pure PVDF-HFP electrospun membrane, the es-CGPEs with one-dimensional AgNWs@SiO_2 inorganic fillers possess a higher ionic conductivity. This AgNWs@SiO_2 can offer continuous ion pathways by uniform permeability networks (Figure 6b). The SiO_2 coated on the surface of AgNWs can improve the long-range ion migration and offer a uniform Li^+ transportation channel between the inorganic filler particle and the polymer chains,[48] which is beneficial to enhancing the ionic conductivity. Besides, the addition of AgNWs@SiO_2 reduces the crystallinity of polymers, which is another important factor for improving the ionic conductivity. The electrochemical stable potential window of the PE is an important parameter for LMBs. Figure 6c shows the LSV curves for the Celgard separator and PVDF-HFP/AgNWs@SiO_2 es-CGPEs. All the membranes display oxidation stabilities up to 4.5 V at 60 °C, indicating that these es-CGPEs could be suitable for use in most commercial cathode materials for LMBs.

The long cycle life, good rate capability, and wide operating temperature of the Li/es-CGPEs/LFP cell are very important for applications in LMBs (Figure 7a). Figures 7b and S5a show the cycling performance of Li/es-CGPEs/LFP operated at 0.5 C at 60 °C. All cells based on es-CGPEs have good cycling stability at 0.5 C after 150 cycles. The initial discharge capacity of the Li//LFP cell assembled with es-CGPEs with 5 wt % AgNWs@SiO_2 at a current density of 0.5 C is 144.4 mA h g^{-1}. The specific capacity reaches 134.1 mA h g^{-1} after 150 cycles (92.9% of capacity retention), and the coulombic efficiency is 99.3%. However, the initial discharge capacities of the Celgard separator (128.4 mA h g^{-1}) and pure PVDF-HFP electrospun membrane (122.5 mA h g^{-1}) are lower, and their discharge capacities exhibit an obvious decay after 150 cycles. The capacity retention is only 63.9 and 66.9% for the Celgard separator and pure PVDF-HFP electrospun membrane, respectively. As shown in Figures 7c, S5b and S6b, Li/es-CGPEs/LFP cells at 60 °C show the outstanding cyclability and rate capability even at 2 C. However, it is observed that the discharge capacity of the cell based on a pure PVDF-HFP

https://doi.org/10.1021/acsaem.1c01420
ACS Appl. Energy Mater. 2021, 4, 8130−8141

electrospun membrane reveals the worst cycling stability and rate capability, and the discharge capacities of the Li/Celgard separator/LFP cell almost reach 0 mA h g^{-1} at 2 C. All these results indicate that the Li/es-CGPEs/LFP cells possess excellent cell cyclability, and the PVDF-HFP/AgNWs@SiO_2 es-CGPEs can be considered as the promising candidate as the PE for the application in LMBs.

Recently, Guo et al.[60] reported that the electrospun PVA nanofiber film (PVANFF) showed a higher thermal conductivity than the value of bulk PVA and the thermal conductivity of PVANFF was also enhanced by doping the AgNWs. Yang et al.[61] reported that the introduction of Al_2O_3 nanoparticles improved the thermal conductivity of the composite separator, which can dissipate heat faster in batteries and decrease temperature rise in operation process. We have shown that the thermal conductivity of epoxy-based composites can be enhanced by adding the AgNWs or AgNWs@SiO_2 into epoxy in our previous studies.[53−55] However, the AgNWs were poorly dispersed in es-CGPEs compared to the AgNWs@SiO_2. Once AgNWs agglomerate in es-CGPEs, the membrane could be punctured and the batteries further lead to short circuit. Thus, the AgNWs@SiO_2 can be considered as the filler candidate to improve the thermal conductivity of PEs membranes. Figure S7a,b suggests the cycling life and rate capability of Li/es-CGPEs/LFP cells at 60 °C by addition of 5 wt % AgNWs and 5 wt % AgNWs@SiO_2 as fillers. It is clearly shown that the es-CGPE with 5 wt % AgNWs@SiO_2 filler possesses the excellent cycling performance and superior high-rate discharge capability at 60 °C. The discharge capacities of the cell based on AgNWs are almost 0 mA h g^{-1} at high rates (1.5 C or 2 C). Figure S8 presents the dispersity of AgNWs and AgNWs@SiO_2 in PVDF-HFP matrix. It can be seen that the AgNWs@SiO_2 can be well dispersed in PVDF-HFP. Consequently, the AgNW agglomerates were probably observed in es-CGPEs and could cause short circuit at 60 °C due to the increased irregular movement. Therefore, the es-CGPEs with AgNWs@SiO_2 demonstrate good cycle performance and excellent rate capability at 60 °C.

To further investigate the cycling performance of the cells based on the electrospun CPMs, the cells were run at 25 °C. Figure 7d depicts charge−discharge curves of the Li/es-CGPEs/LFP battery based on the electrospun membrane with 5 wt % AgNWs@SiO_2 loading under a certain current density as 0.5 C at 25 °C. The specific capacity difference between the charging and discharging process is very small, indicating the formation of stabilization of interface through the reversible reaction.[62,63] Figures 7e and S5c show the cycling performance of Li/es-CGPEs/LFP cells operated at 0.5 C at 25 °C. It is seen that all membranes have good cycling stability at 0.5 C after 150 cycles at 25 °C, and the cycling performance is greatly enhanced when using es-CGPEs. Among them, the cell based on es-CGPEs with 5 wt % of AgNWs@SiO_2 displays the best cycling performance. The initial discharge capacity is 142.4 mA h g^{-1}, and the discharge capacity still remains as high as 125.1 mA h g^{-1} after 150 cycles (coulombic efficiency nearly 100%). Meanwhile, the cell based on es-CGPEs with 5 wt % of AgNWs@SiO_2 also offers good cycling stability at 1 C after 150 cycles at 25 °C (Figure S9a). The elements of Fe and P can be found at a cycled separator (Figure S9b), and the cycled separator still remains a stable nanofiber structure (Figure S9c). Figures 7f and S6a illustrate the rate capability of the cell at different C-rates of 0.2 C, 0.5 C, 1 C, 1.5 C, and 2 C at 25 °C in the case of 5 wt % of AgNWs@SiO_2. The discharge specific capacities of the cell are 142.0, 112.9, 104.5, and 96.7 mA h g^{-1} remain when the current densities are 0.5 C, 1 C, 1.5 C, and 2 C, respectively, which are at around 96.6, 76.8, 71.1, and 65.8% of the capacity at 0.2 C (147.0 mA h g^{-1}). Therefore, AgNWs@SiO_2 is an excellent candidate as the inorganic filler for designing organic−inorganic hybrid PE membranes. Figures 7f and S5d display the rate performance of the cells at 25 °C at different C-rates. It can be found that the es-CGPEs with AgNWs@SiO_2 can clearly improve rate capability. As investigated above, the electrospun composite PEs with AgNWs@SiO_2 have higher ionic conductivities and good mechanical strength, which is beneficial to contributing the cycling performance. Moreover, the Li/es-CGPEs/LFP cells show a reversible discharge capacity at 0.5 C after five cycles at 2 C, indicating the outstanding rate performance of Li/es-CGPEs/LFP cells. Also, the discharge capacities in all es-CGPE cells are higher than the Celgard separator system. However, the discharge capacities of the Li/PVDF-HFP/LFP cell are very low at high current densities, suggesting the advantage of the AgNWs@SiO_2 loading. Besides, the ion conduction is restricted in the pure PVDF-HFP electrospun membrane with very high mechanical strength (Figure S10), resulting in poor high-rate performance. In view of the abovementioned results, the LMBs assembled with the es-CGPE with 5 wt % of AgNWs@SiO_2 exhibit good cycling stability and superior rate performance at a wide temperature range.

Figure S11a shows the cycling performance of Li//LFP cells based on the es-CGPEs with 5 wt % AgNWs and 5 wt % AgNWs@SiO_2 as fillers, and a superior cycling stability could be observed at 0.5 C at 25 °C. Figure S11b reveals the rate performance of the cell at 25 °C, the discharge specific capacities of the cell with 5 wt % of AgNWs are 146.3, 135.9, 126.8, 119.7, and 112.5 mA h g^{-1} under the current density are 0.2 C, 0.5 C, 1 C, 1.5 C, and 2 C, respectively. It can be seen that 5 wt % of AgNWs have better high-rate performance from 1 C to 2 C at 25 °C. The main reasons may be as follows: Not only the higher thermal conductivity can be obtained by addition of 5 wt % AgNWs in es-CGPEs but also the more AgNWs fillers in es-CGPEs will help in the migration of lithium ions at high-rate charge/discharge testing. As shown in Table S2, these results show that the AgNWs or AgNWs@SiO_2 is beneficial to improve the electrochemical performance of the battery at 25 °C.

To demonstrate the feasibility of the es-CGPEs employed at an extreme operating condition, the Li/es-CGPEs/LFP cell based on the es-CGPE with 5 wt % AgNWs@SiO_2 was assembled, and the cycling stability and charge−discharge performances at various rates were examined at 0 °C. Figure 7g depicts the cycle stability of the Li/es-CGPEs/LFP cell at 0.5 C. It is noted that the Li/es-CGPEs/LFP cell displays good cycle durability at 0 °C after 500 cycles, which is attributed to the good electrochemically interfacial stability. Besides, the cell assembled with es-CGPEs with 5 wt % of AgNWs@SiO_2 still delivers an excellent C-rate capability at 0 °C (Figure 7h), further indicating the reliability of es-CGPEs. The good rate performance leads to better ionic transport capability. Notably, the discharge capacity of the cell assembled with the es-CGPE based on 5 wt % AgNWs@SiO_2 at 25 °C is even higher than that of the Celgard separator and pure electrospun PVDF-HFP membrane at 60 °C (Figure S5f). These results show the Li/es-CGPEs/LFP cell with es-CGPE based on 5 wt % AgNWs@

https://doi.org/10.1021/acsaem.1c01420
ACS Appl. Energy Mater. 2021, 4, 8130−8141

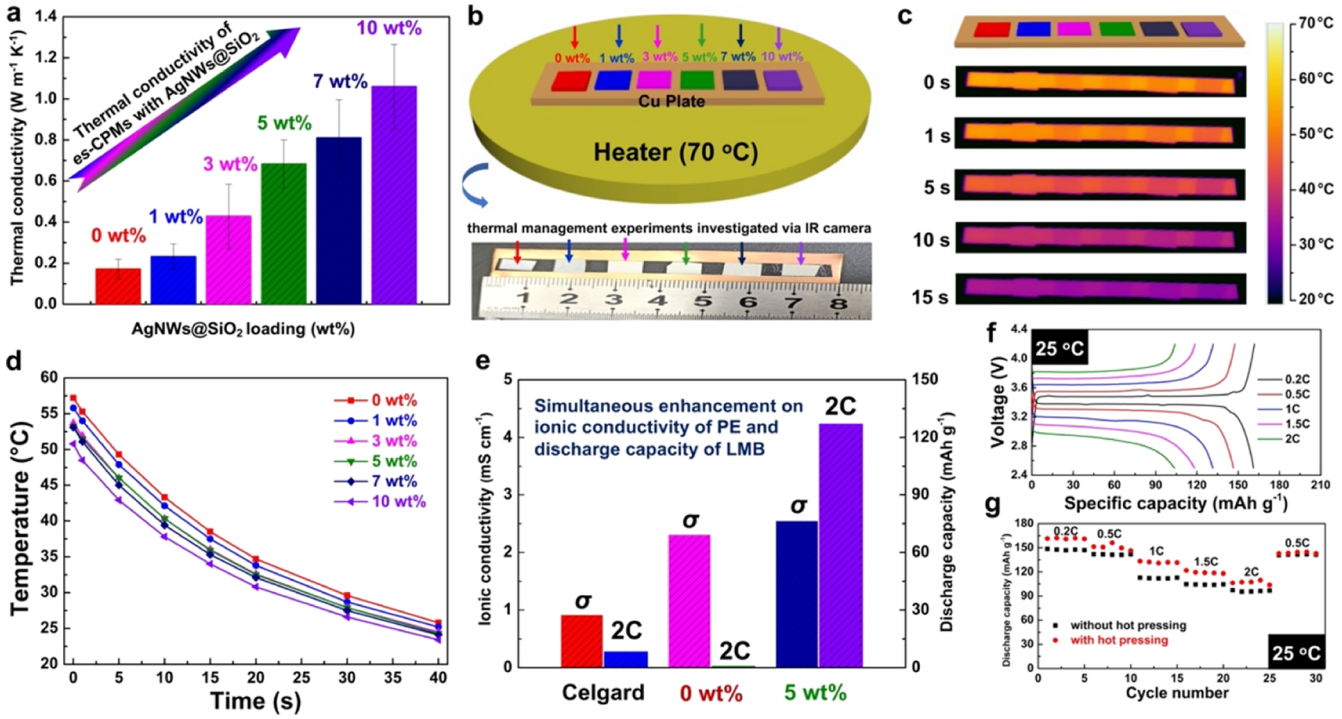

Figure 8. (a) Thermal conductivities of hot-pressed es-CPMs versus loading of AgNWs@SiO_2. (b) Schematic illustration of the thermal management experiment of hot-pressed es-CPMs by using an IR camera. (c) IR images of hot-pressed es-CPMs. (d) Temperature−time curves of hot-pressed es-CPMs. (e) Ionic conductivity (60 °C) of the Celgard separator and es-CGPEs with 0 or 5 wt % of AgNWs@SiO_2 and discharge capacity of LMBs at 2 C at 60 °C. (f) Charge−discharge curves of Li//LFP assembled with es-CGPEs with 5 wt % of AgNWs@SiO_2 at different rates with hot-pressed es-CGPEs at 25 °C. (g) Rate performance of Li//LFP assembled with or without hot-pressed es-CGPEs with 5 wt % of AgNWs@SiO_2 at different rates of 0.2, 0.5, 1, 1.5, and 2 C at 25 °C.

SiO_2 exhibits superior cycling stability and excellent rate capability at a wide temperature range.

Generally, PEs have an ultralow thermal conductivity. Then, the thermal variation across the PEs results in the nonuniformity in the ionic conductivity. The thermal conduction properties of es-CPMs are measured by the 3ω method and analyzed by a bidirectional asymmetric heat transfer model, which has been successfully used in studying the thermal conductivity of polymer films,[64] nanowire arrays,[65] and metal inverse opals.[66] The two-layer es-CPMs were stacked together by a hot pressing method for the accurate test of thermal conductivity. As shown in Figure 8a, it is clear that the thermal conductivity (κ) of hot-pressed es-CPMs increases with increasing AgNWs@SiO_2. The values of κ are 0.17 ± 0.04, 0.23 ± 0.06, 0.42 ± 0.15, 0.68 ± 0.11, 0.81 ± 0.18, and 1.06 ± 0.20 W m^{-1} K^{-1}, corresponding to 0, 1, 3, 5, 7, and 10 wt % of AgNWs@SiO_2, respectively.

As investigated above, the mechanical properties of PEs were improved importantly by the incorporation of AgNWs@SiO_2 into the polymer matrix (Figure 4d). Interestingly, the AgNWs@SiO_2 also promotes the thermal conductivities of es-CPMs, which could result in a faster equalization of heat variation in the es-CGPE. The es-CGPEs with AgNWs@SiO_2 also present a higher ionic conductivity and more homogenous lithium-ion transport upon a temperature change compared to the electrolytes without the loading of AgNWs@SiO_2 (Figure 6a). Although the sample with 7 or 10 wt % of AgNWs@SiO_2 exhibits a higher κ value than 5 wt % of AgNWs@SiO_2, the low content of PVDF-HFP shows that the es-CPMs have a poor mechanical strength (Figure 4d). The faster thermal response of the es-CPMs with AgNWs@SiO_2 will lead to a fast stabilization of discharge potentials in the LMBs when various temperatures are employed. Therefore, the obtained hot-pressed es-CPMs with 5 wt % of AgNWs@SiO_2 were assembled into CR2032 coin cells to further study the cycle performance and rate capability of LMBs.

The thermal management experiments of two-layer es-CPMs were observed by the infrared camera (Fotric 226s IR camera). As shown in Figure 8b, the hot-pressed es-CPMs were put on the surface of a Cu plate. The Cu plate was then heated by the heater from room temperature to 70 °C. When the temperature of the Cu plate was stabilized at 70 °C for several minutes, the Cu plate was quickly put under the infrared camera to take images. A distinctive difference of temperature distribution can be observed in Figure 8c with the increasing loading of AgNWs@SiO_2 in es-CPMs. Notably, the accelerated thermal conduction was observed when AgNWs@SiO_2 were introduced into the es-CPMs. As shown in Figure 8d, the temperature was apparently decreased with increasing AgNWs@SiO_2 in es-CPMs. These results indicate that AgNWs@SiO_2 is the suitable inorganic filler candidate for the thermal conduction to enhance the thermal conductivity of es-CPMs. The high thermal conductivity of es-CPMs with AgNWs@SiO_2 is also beneficial to improve the ionic conductivity of PEs and the cycling performance of LMBs, especially at a higher temperature (Figure 8e).

To further evaluate cycling stability of hot-pressed es-CPMs, Li//Li symmetric cells were explored by Li/es-CGPEs/Li based on 5 wt % AgNWs@SiO_2 at a constant current density of 0.5 mA cm^{-2} at 60 °C. Figure S12a shows that the symmetric cell possesses an ultralow initial overpotential of only below 10 mV (Figure S12b) and exhibits good stable

https://doi.org/10.1021/acsaem.1c01420
ACS Appl. Energy Mater. 2021, 4, 8130−8141

cycle performance for 200 h (100 cycles), suggesting that hot-pressed es-CPMs still maintain good interfacial stability between the Li metal anode. The es-CGPEs with 5 wt % AgNWs@SiO_2 are conducive to controlling Li nucleation, inhibiting Li dendrite growth, and improving the electrochemical performance (Figure S13). The as-prepared hot-pressed es-CPMs with 5 wt % of AgNWs@SiO_2 are employed as the separator, and the cells are run at different temperatures for all cases. Figure 8f displays charge−discharge curves at different rates with hot-pressed es-CGPEs at 25 °C, and the discharge specific capacities of the cell are 161.1, 146.5, 131.6, 118.1, and 103.7 mA h g^{-1} under the current density are 0.2 C, 0.5 C, 1 C, 1.5 C, and 2 C, respectively. Figure 8g shows the rate performance of cells at 25 °C, and the hot-pressed es-CGPE with 5 wt % AgNWs@SiO_2 exhibits better rate capability than the hot-pressed es-CGPE without it. Figure S12c shows the charge−discharge curves at different rates with hot-pressed es-CGPEs at 0 °C, and the discharge specific capacities of the cell are 88.3, 68.9, 55.2, 46.5, and 39.5 mA h g^{-1} under the current densities 0.2 C, 0.5 C, 1 C, 1.5 C, and 2 C, respectively. Figure S12d shows the rate performance of cells at 0 °C, and the hot-pressed es-CGPE with 5 wt % AgNWs@SiO_2 exhibits outstanding discharge specific capacities at high rates (1.5 C or 2 C). Thus, these results indicate that the two-layer es-CPMs exhibit a good rate capability and that the hot-pressed method has a promising potential for the application of the obtained multilayer separator in the future.

CONCLUSIONS

In summary, the electrospun CPMs (es-CPMs) based on PVDF-HFP and AgNWs@SiO_2 were fabricated. The AgNWs@SiO_2 can act as a promising one-dimensional inorganic filler to enhance the physical and electrochemical performances. The es-CPMs offer high thermal and dimensional stabilities, high thermal conductivity, good wettability, high porosity, and excellent mechanical strength. The decomposition temperature of es-CPMs is above 400 °C and exhibits the good dimensional stability at 120 °C for 12 h, which is superior to the Celgard separator. The as-formed PVDF-HFP/AgNWs@SiO_2 es-CGPEs have a wide stable potential window, good cycling stability, and excellent rate capability in a wide temperature range. These results demonstrate that the es-CGPEs are the promising electrolytes, and this work also boosts the development of high-performance LMBs..

ASSOCIATED CONTENT

Supporting Information

The Supporting Information is available free of charge at https://pubs.acs.org/doi/10.1021/acsaem.1c01420.

Diameter distributions of PVDF-HFP/AgNWs@SiO_2 es-CPMs fibers; N_2 adsorption/desorption isotherms and BJH pore size distribution of PVDF-HFP/AgNWs@SiO_2 es-CPMs fibers; pore area and pore size distribution of PVDF-HFP/AgNWs@SiO_2 es-CPMs fibers; information of stress, strain, heat of fusion (ΔH), crystallinity (X_c), and ionic conductivity for PVDF-HFP/AgNWs@SiO_2 es-CPMs; FT-IR spectra of PVDF-HFP/AgNWs@SiO_2 es-CPMs, cycling performance and rate performance of Li/es-CGPEs/LFP cells operated at different rates and temperatures; discharge curves of Li/es-CGPEs/LFP cells; cycling performance and rate performance of Li/es-CGPEs/LFP cells assembled with PEs based on AgNWs or AgNWs@SiO_2; dispersity of AgNWs and AgNWs@SiO_2 in the PVDF-HFP matrix; cycling performance of Li/es-CGPEs/LFP cells, EDAX spectrum of the separator before and after cycling, SEM images of the separator after cycling; stress−strain curves of the Celgard separator; cycling performance and rate performance of Li/es-CGPEs/LFP cells assembled with PEs based on AgNWs or AgNWs@SiO_2; comparison of discharge capacity of the Li//LFP cell at different rates and cycling performance at 25°C; voltage−time curves of Li/es-CGPEs/Li symmetric cells, enlarged voltage−time profiles at 100-120 h, charge−discharge curves of the Li//LFP cell at different rates, rate performance of Li//LFP assembled with or without S10 hot-pressed es-CGPEs; and voltage−time curves of Li/es-CGPEs/Li symmetric cells (PDF)

AUTHOR INFORMATION

Corresponding Authors

Ji Hu − *School of Materials Science and Engineering, Luoyang Institute of Science and Technology, Luoyang 471023, China*; Email: jhu@lit.edu.cn

Nuo Yang − *State Key Laboratory of Coal Combustion, and School of Energy and Power Engineering, Huazhong University of Science and Technology, Wuhan 430074, P. R. China*; orcid.org/0000-0003-0973-1718; Email: nuo@hust.edu.cn

Zhigang Xue − *Key Laboratory of Material Chemistry for Energy Conversion and Storage, Ministry of Education, Hubei Key Laboratory of Material Chemistry and Service Failure, School of Chemistry and Chemical Engineering, Huazhong University of Science and Technology, Wuhan 430074, China*; orcid.org/0000-0003-2335-9537; Email: zgxue@mail.hust.edu.cn

Authors

Huihui Gan − *Key Laboratory of Material Chemistry for Energy Conversion and Storage, Ministry of Education, Hubei Key Laboratory of Material Chemistry and Service Failure, School of Chemistry and Chemical Engineering, Huazhong University of Science and Technology, Wuhan 430074, China*

Jiale Yuan − *State Key Laboratory of Coal Combustion, and School of Energy and Power Engineering, Huazhong University of Science and Technology, Wuhan 430074, P. R. China*

Yong Zhang − *Key Laboratory of Material Chemistry for Energy Conversion and Storage, Ministry of Education, Hubei Key Laboratory of Material Chemistry and Service Failure, School of Chemistry and Chemical Engineering, Huazhong University of Science and Technology, Wuhan 430074, China*

Shaoqiao Li − *Key Laboratory of Material Chemistry for Energy Conversion and Storage, Ministry of Education, Hubei Key Laboratory of Material Chemistry and Service Failure, School of Chemistry and Chemical Engineering, Huazhong University of Science and Technology, Wuhan 430074, China*

Liping Yu − *Key Laboratory of Material Chemistry for Energy Conversion and Storage, Ministry of Education, Hubei Key Laboratory of Material Chemistry and Service Failure, School of Chemistry and Chemical Engineering, Huazhong University of Science and Technology, Wuhan 430074, China*

https://doi.org/10.1021/acsaem.1c01420
ACS Appl. Energy Mater. 2021, 4, 8130−8141

Jirong Wang − *Key Laboratory of Material Chemistry for Energy Conversion and Storage, Ministry of Education, Hubei Key Laboratory of Material Chemistry and Service Failure, School of Chemistry and Chemical Engineering, Huazhong University of Science and Technology, Wuhan 430074, China*

Complete contact information is available at: https://pubs.acs.org/10.1021/acsaem.1c01420

Author Contributions

‖H.G. and J.Y. contributed equally to this work.

Notes

The authors declare no competing financial interest.

■ ACKNOWLEDGMENTS

We are grateful to the National Natural Science Foundation of China (51973073), Science and Technology Department of Henan Province of China (192102210184), Applied and Fundamental Frontier Program of Wuhan (2019010701011409), and The Innovation and Talent Recruitment Base of New Energy Chemistry and Device (B21003) for support of this work. The authors also gratefully acknowledge the Analytical and Testing Center of Huazhong University of Science and Technology for measurements.

■ REFERENCES

(1) Armand, M.; Tarascon, J.-M. Building Better Batteries. *Nature* **2008**, *451*, 652−657.
(2) Winter, M.; Barnett, B.; Xu, K. Before Li Ion Batteries. *Chem. Rev.* **2018**, *118*, 11433−11456.
(3) Nayak, P. K.; Yang, L.; Brehm, W.; Adelhelm, P. From Lithium-Ion to Sodium-Ion Batteries: Advantages, Challenges, and Surprises. *Angew. Chem., Int. Ed.* **2018**, *57*, 102−120.
(4) Wang, X.; Kerr, R.; Chen, F.; Goujon, N.; Pringle, J. M.; Mecerreyes, D.; Forsyth, M.; Howlett, P. C. Toward High-Energy-Density Lithium Metal Batteries: Opportunities and Challenges for Solid Organic Electrolytes. *Adv. Mater.* **2020**, *32*, 1905219.
(5) Griffith, K. J.; Wiaderek, K. M.; Cibin, G.; Marbella, L. E.; Grey, C. P. Niobium Tungsten Oxides for High-Rate Lithium-Ion Energy Storage. *Nature* **2018**, *559*, 556−563.
(6) Gong, C.; Xue, Z.; Wen, S.; Ye, Y.; Xie, X. Advanced Carbon Materials/Olivine $LiFePO_4$ Composites Cathode for Lithium Ion Batteries. *J. Power Sources* **2016**, *318*, 93−112.
(7) Tang, W.; Zhou, G.; Cao, J.; Chen, Z.; Yang, Z.; Huang, H.; Qu, Y.; Li, C.; Zhang, W.; Liu, H. Recent Advances of Mesoscale-Structured Cathode Materials for High Energy Density Lithium-Ion Batteries. *ACS Appl. Energy Mater.* **2021**, *4*, 2962−2975.
(8) Xue, Z.; He, D.; Xie, X. Poly(ethylene oxide)-Based Electrolytes for Lithium-Ion Batteries. *J. Mater. Chem. A* **2015**, *3*, 19218−19253.
(9) Liang, P.; Shao, G.; Wang, H.; Wang, C.-a. In Situ Electrode Stress Monitoring: An Effective Approach to Study the Electrochemical Behavior of a Lithium Metal Anode. *ACS Appl. Energy Mater.* **2021**, *4*, 3993−4001.
(10) Lopez, J.; Mackanic, D. G.; Cui, Y.; Bao, Z. Designing Polymers for Advanced Battery Chemistries. *Nat. Rev. Mater.* **2019**, *4*, 312−330.
(11) Cheng, X.-B.; Zhao, C.-Z.; Yao, Y.-X.; Liu, H.; Zhang, Q. Recent Advances in Energy Chemistry between Solid-State Electrolyte and Safe Lithium-Metal Anodes. *Chem* **2019**, *5*, 74−96.
(12) Bouchet, R.; Maria, S.; Meziane, R.; Aboulaich, A.; Lienafa, L.; Bonnet, J.-P.; Phan, T. N. T.; Bertin, D.; Gigmes, D.; Devaux, D.; Denoyel, R.; Armand, M. Single-Ion BAB Triblock Copolymers as Highly Efficient Electrolytes for Lithium-Metal Batteries. *Nat. Mater.* **2013**, *12*, 452−457.
(13) Liu, B.; Zhang, J.-G.; Xu, W. Advancing Lithium Metal Batteries. *Joule* **2018**, *2*, 833−845.
(14) Xiao, J.; Li, Q.; Bi, Y.; Cai, M.; Dunn, B.; Glossmann, T.; Liu, J.; Osaka, T.; Sugiura, R.; Wu, B.; Yang, J.; Zhang, J.-G.; Whittingham, M. S. Understanding and Applying Coulombic Efficiency in Lithium Metal Batteries. *Nat. Energy* **2020**, *5*, 561−568.
(15) Zachman, M. J.; Tu, Z.; Choudhury, S.; Archer, L. A.; Kourkoutis, L. F. Cryo-STEM Mapping of Solid-Liquid Interfaces and Dendrites in Lithium-Metal Batteries. *Nature* **2018**, *560*, 345−349.
(16) Fang, C.; Li, J.; Zhang, M.; Zhang, Y.; Yang, F.; Lee, J. Z.; Lee, M.-H.; Alvarado, J.; Schroeder, M. A.; Yang, Y.; Lu, B.; Williams, N.; Ceja, M.; Yang, L.; Cai, M.; Gu, J.; Xu, K.; Wang, X.; Meng, Y. S. Quantifying Inactive Lithium in Lithium Metal Batteries. *Nature* **2019**, *572*, 511−515.
(17) Tang, W.; Yin, X.; Kang, S.; Chen, Z.; Tian, B.; Teo, S. L.; Wang, X.; Chi, X.; Loh, K. P.; Lee, H.-W.; Zheng, G. W. Lithium Silicide Surface Enrichment: A Solution to Lithium Metal Battery. *Adv. Mater.* **2018**, *30*, 1801745.
(18) Phattharasupakun, N.; Wutthiprom, J.; Duangdangchote, S.; Sawangphruk, M. A 3D Free-Standing Lithiophilic Silver Nanowire Aerogel for Lithium Metal Batteries without Lithium Dendrites and Volume Expansion: In Operand X-ray Diffraction. *Chem. Commun.* **2019**, *55*, 5689−5692.
(19) Zhao, Q.; Hao, X.; Su, S.; Ma, J.; Hu, Y.; Liu, Y.; Kang, F.; He, Y.-B. Expanded-Graphite Embedded in Lithium Metal as Dendrite-Free Anode of Lithium Metal Batteries. *J. Mater. Chem. A* **2019**, *7*, 15871−15879.
(20) Ghazi, Z. A.; Sun, Z.; Sun, C.; Qi, F.; An, B.; Li, F.; Cheng, H.-M. Key Aspects of Lithium Metal Anodes for Lithium Metal Batteries. *Small* **2019**, *15*, 1900687.
(21) Sun, X.; Zhang, X.; Ma, Q.; Guan, X.; Wang, W.; Luo, J. Revisiting the Electroplating Process for Lithium-Metal Anodes for Lithium-Metal Batteries. *Angew. Chem., Int. Ed.* **2020**, *59*, 6665−6674.
(22) Zhu, Y.; Xie, J.; Pei, A.; Liu, B.; Wu, Y.; Lin, D.; Li, J.; Wang, H.; Chen, H.; Xu, J.; Yang, A.; Wu, C.-L.; Wang, H.; Chen, W.; Cui, Y. Fast Lithium Growth and Short Circuit Induced by Localized-Temperature Hotspots in Lithium Batteries. *Nat. Commun.* **2019**, *10*, 2067.
(23) Moon, S.; Tamwattana, O.; Park, H.; Yoon, G.; Seong, W. M.; Lee, M. H.; Park, K.-Y.; Meethong, N.; Kang, K. A Bifunctional Auxiliary Electrode for Safe Lithium Metal Batteries. *J. Mater. Chem. A* **2019**, *7*, 24807−24813.
(24) Jin, T.; Wang, Y.; Hui, Z.; Qie, B.; Li, A.; Paley, D.; Xu, B.; Wang, X.; Chitu, A.; Zhai, H.; Gong, T.; Yang, Y. Nonflammable, Low-Cost, and Fluorine-Free Solvent for Liquid Electrolyte of Rechargeable Lithium Metal Batteries. *ACS Appl. Mater. Interfaces* **2019**, *11*, 17333−17340.
(25) Shen, K.; Wang, Z.; Bi, X.; Ying, Y.; Zhang, D.; Jin, C.; Hou, G.; Cao, H.; Wu, L.; Zheng, G.; Tang, Y.; Tao, X.; Lu, J. Magnetic Field-Suppressed Lithium Dendrite Growth for Stable Lithium-Metal Batteries. *Adv. Energy Mater.* **2019**, *9*, 1900260.
(26) Ren, W.; Zheng, Y.; Cui, Z.; Tao, Y.; Li, B.; Wang, W. Recent Progress of Functional Separators in Dendrite Inhibition for Lithium Metal Batteries. *Energy Storage Mater.* **2021**, *35*, 157−168.
(27) Kim, M. S.; Ryu, J.-H.; Deepika; Lim, Y. R.; Nah, I. W.; Lee, K.-R.; Archer, L. A.; Cho, W. I. Langmuir-Blodgett Artificial Solid-Electrolyte Interphases for Practical Lithium Metal Batteries. *Nat. Energy* **2018**, *3*, 889−898.
(28) Tikekar, M. D.; Choudhury, S.; Tu, Z. Y.; Archer, L. A. Design Principles for Electrolytes and Interfaces for Stable Lithium-Metal Batteries. *Nat. Energy* **2016**, *1*, 16114.
(29) Zhang, X.-Q.; Li, T.; Li, B.-Q.; Zhang, R.; Shi, P.; Yan, C.; Huang, J.-Q.; Zhang, Q. A Sustainable Solid Electrolyte Interphase for High-Energy-Density Lithium Metal Batteries Under Practical Conditions. *Angew. Chem., Int. Ed.* **2020**, *132*, 3278−3283.
(30) Wang, D.; Liu, H.; Li, M.; Xia, D.; Holoubek, J.; Deng, Z.; Yu, M.; Tian, J.; Shan, Z.; Ong, S. P.; Liu, P.; Chen, Z. A Long-Lasting Dual-Function Electrolyte Additive for Stable Lithium Metal Batteries. *Nano Energy* **2020**, *75*, 104889.
(31) Lin, D.; Zhuo, D.; Liu, Y.; Cui, Y. All-Integrated Bifunctional Separator for Li Dendrite Detection via Novel Solution Synthesis of a Thermostable Polyimide Separator. *J. Am. Chem. Soc.* **2016**, *138*, 11044−11050.

(32) Yue, H.; Zhu, Q.; Dong, S.; Zhou, Y.; Yang, Y.; Cheng, L.; Qian, M.; Liang, L.; Wei, W.; Wang, H. Nanopile Interlocking Separator Coating toward Uniform Li Deposition of the Li Metal Anodes. *ACS Appl. Mater. Interfaces* **2020**, *12*, 43543−43552.
(33) Wang, J.; Li, S.; Zhao, Q.; Song, C.; Xue, Z. Structure Code for Advanced Polymer Electrolyte in Lithium-Ion Batteries. *Adv. Funct. Mater.* **2020**, *31*, 2008208.
(34) Guan, T.; Rong, Z.; Cheng, F.; Zhang, W.; Chen, J. UV-Cured Interpenetrating Networks of Single-ion Conducting Polymer Electrolytes for Rechargeable Lithium Metal Batteries. *ACS Appl. Energy Mater.* **2020**, *3*, 12532−12539.
(35) Ren, W.; Ding, C.; Fu, X.; Huang, Y. Advanced Gel Polymer Electrolytes for Safe and Durable Lithium Metal Batteries: Challenges, Strategies, and Perspectives. *Energy Storage Mater.* **2021**, *34*, 515−535.
(36) Jie, J.; Liu, Y.; Cong, L.; Zhang, B.; Lu, W.; Zhang, X.; Liu, J.; Xie, H.; Sun, L. High-Performance PVDF-HFP Based Gel Polymer Electrolyte with a Safe Solvent in Li Metal Polymer Battery. *J. Energy Chem.* **2020**, *49*, 80−88.
(37) Choi, S. W.; Kim, J. R.; Ahn, Y. R.; Jo, S. M.; Cairns, E. J. Characterization of Electrospun PVdF Fiber-Based Polymer Electrolytes. *Chem. Mater.* **2007**, *19*, 104−115.
(38) Akashi, H.; Shibuya, M.; Orui, K.; Shibamoto, G.; Sekai, K. Practical Performances of Li-Ion Polymer Batteries with Li-$Ni_{0.8}Co_{0.2}O_2$, MCMB, and PAN-Based Gel Electrolyte. *J. Power Sources* **2002**, *112*, 577−582.
(39) Hao, J.; Lei, G.; Li, Z.; Wu, L.; Xiao, Q.; Wang, L. A Novel Polyethylene Terephthalate Nonwoven Separator Based on Electrospinning Technique for Lithium Ion Battery. *J. Membr. Sci.* **2013**, *428*, 11−16.
(40) Li, Z.; Wang, W.; Han, Y.; Zhang, L.; Li, S.; Tang, B.; Xu, S.; Xu, Z. Ether Modified Poly(ether ether ketone) Nonwoven Membrane with Excellent Wettability and Stability as a Lithium Ion Battery Separator. *J. Power Sources* **2018**, *378*, 176−183.
(41) Quartarone, E.; Tomasi, C.; Mustarelli, P.; Appetecchi, G. B.; Croce, F. Long-Term Structural Stability of PMMA-Based Gel Polymer Electrolytes. *Electrochim. Acta* **1998**, *43*, 1435−1439.
(42) Li, W.; Pang, Y.; Liu, J.; Liu, G.; Wang, Y.; Xia, Y. A PEO-Based Gel Polymer Electrolyte for Lithium Ion Batteries. *RSC Adv.* **2017**, *7*, 23494−23501.
(43) Lee, Y.-S.; Lee, J. H.; Choi, J.-A.; Yoon, W. Y.; Kim, D.-W. Cycling Characteristics of Lithium Powder Polymer Batteries Assembled with Composite Gel Polymer Electrolytes and Lithium Powder Anode. *Adv. Funct. Mater.* **2013**, *23*, 1019−1027.
(44) Xu, D.; Su, J.; Jin, J.; Sun, C.; Ruan, Y.; Chen, C.; Wen, Z. In Situ Generated Fireproof Gel Polymer Electrolyte with $Li_{6.4}Ga_{0.2}La_3Zr_2O_{12}$ as Initiator and Ion-Conductive Filler. *Adv. Energy Mater.* **2019**, *9*, 1900611.
(45) Wu, C.-G.; Lu, M.-I.; Tsai, C.-C.; Chuang, H.-J. PVdF-HFP/Metal Oxide Nanocomposites: The Matrices for High-Conducting, Low-Leakage Porous Polymer Electrolytes. *J. Power Sources* **2006**, *159*, 295−300.
(46) Yang, C.-C.; Lian, Z.-Y.; Lin, S. J.; Shih, J.-Y.; Chen, W.-H. Preparation and Application of PVDF-HFP Composite Polymer Electrolytes in $LiNi_{0.5}Co_{0.2}Mn_{0.3}O_2$ Lithium-Polymer Batteries. *Electrochim. Acta* **2014**, *134*, 258−265.
(47) Padmaraj, O.; Nageswara Rao, B.; Jena, P.; Venkateswarlu, M.; Satyanarayana, N. Electrochemical Studies of Electrospun Organic/Inorganic Hybrid Nanocomposite Fibrous Polymer Electrolyte for Lithium Battery. *Polymer* **2014**, *55*, 1136−1142.
(48) Lei, D.; He, Y.-B.; Huang, H.; Yuan, Y.; Zhong, G.; Zhao, Q.; Hao, X.; Zhang, D.; Lai, C.; Zhang, S.; Ma, J.; Wei, Y.; Yu, Q.; Lv, W.; Yu, Y.; Li, B.; Yang, Q.-H.; Yang, Y.; Lu, J.; Kang, F. Cross-Linked Beta Alumina Nanowires with Compact Gel Polymer Electrolyte Coating for Ultra-Stable Sodium Metal Battery. *Nat. Commun.* **2019**, *10*, 4244.
(49) Xiao, W.; Li, X.; Guo, H.; Wang, Z.; Zhang, Y.; Zhang, X. Preparation of Core-Shell Structural Single Ionic Conductor SiO_2@Li^+ and Its Application in PVDF-HFP-Based Composite Polymer Electrolyte. *Electrochim. Acta* **2012**, *85*, 612−621.
(50) Liu, Y.; Qiao, Y.; Zhang, Y.; Yang, Z.; Gao, T.; Kirsch, D.; Liu, B.; Song, J.; Yang, B.; Hu, L. 3D printed Separator for the Thermal Management of High-Performance Li Metal Anodes. *Energy Storage Mater.* **2018**, *12*, 197−203.
(51) Luo, W.; Zhou, L.; Fu, K.; Yang, Z.; Wan, J.; Manno, M.; Yao, Y.; Zhu, H.; Yang, B.; Hu, L. A Thermally Conductive Separator for Stable Li Metal Anodes. *Nano Lett.* **2015**, *15*, 6149−6154.
(52) Yin, X.; Wang, L.; Kim, Y.; Ding, N.; Kong, J.; Safanama, D.; Zheng, Y.; Xu, J.; Repaka, D. V. M.; Hippalgaonkar, K.; Lee, S. W.; Adams, S.; Zheng, G. W. Thermal Conductive 2D Boron Nitride for High-Performance All-Solid-State Lithium-Sulfur Batteries. *Adv. Sci.* **2020**, *7*, 2001303.
(53) Chen, C.; Wang, H.; Xue, Y.; Xue, Z.; Liu, H.; Xie, X.; Mai, Y.-W. Structure, Rheological, Thermal Conductive and Electrical Insulating Properties of High-Performance Hybrid Epoxy/Nano-silica/AgNWs Nanocomposites. *Compos. Sci. Technol.* **2016**, *128*, 207−214.
(54) Chen, C.; Tang, Y.; Ye, Y. S.; Xue, Z.; Xue, Y.; Xie, X.; Mai, Y.-W. High-Performance Epoxy/Silica Coated Silver Nanowire Composites as Underfill Material for Electronic Packaging. *Compos. Sci. Technol.* **2014**, *105*, 80−85.
(55) Jiang, Y.; Li, M.; Chen, C.; Xue, Z.; Xie, X.; Zhou, X.; Mai, Y.-W. Effect of Elastic Modulus Mismatch of Epoxy/Titanium Dioxide Coated Silver Nanowire Composites on the Performance of Thermal Conductivity. *Compos. Sci. Technol.* **2018**, *165*, 206−213.
(56) Cahill, D. G. Thermal Conductivity Measurement from 30 to 750 K: the 3ω Method. *Rev. Sci. Instrum.* **1990**, *61*, 802−808.
(57) Lee, S.-M.; Cahill, D. G. Heat Transport in Thin Dielectric Films. *J. Appl. Phys.* **1997**, *81*, 2590−2595.
(58) Liang, X.; Yu, S.; Sun, R.; Luo, S.; Wan, J. Microstructure and Dielectric Behavior of the Three-Phase Ag@SiO_2/$BaTiO_3$/PVDF Composites with High Permittivity. *J. Mater. Res.* **2012**, *27*, 991−998.
(59) Solarajan, A. K.; Murugadoss, V.; Angaiah, S. Montmorillonite Embedded Electrospun PVdF-HFP Nanocomposite Membrane Electrolyte for Li-Ion Capacitors. *Appl. Mater. Today* **2016**, *5*, 33−40.
(60) Guo, L.; Chen, X.; Tang, N.; Chen, C.; Deng, S.; Li, X.; Zang, J.; Xue, Z.; Yang, N. Enhancement of Thermal Conductivity of Electrospinning PVA Nano-Fiber Film by Doping Silver Nanowires. *Abstract of the 16th International Heat Transfer Conference in Beijing*, 2018; pp 6947−6954.
(61) Yang, Y.; Huang, X.; Cao, Z.; Chen, G. Thermally Conductive Separator with Hierarchical Nano/Microstructures for Improving Thermal Management of Batteries. *Nano Energy* **2016**, *22*, 301−309.
(62) Jo, Y. H.; Li, S.; Zuo, C.; Zhang, Y.; Gan, H.; Li, S.; Yu, L.; He, D.; Xie, X.; Xue, Z. Self-Healing Solid Polymer Electrolyte Facilitated by a Dynamic Cross-Linked Polymer Matrix for Lithium-Ion Batteries. *Macromolecules* **2020**, *53*, 1024−1032.
(63) Zhou, B.; Yang, M.; Zuo, C.; Chen, G.; He, D.; Zhou, X.; Liu, C.; Xie, X.; Xue, Z. Flexible, Self-Healing, and Fire-Resistant Polymer Electrolytes Fabricated via Photopolymerization for All-Solid-State Lithium Metal Batteries. *ACS Macro Lett.* **2020**, *9*, 525−532.
(64) Coates, N. E.; Yee, S. K.; McCulloch, B.; See, K. C.; Majumdar, A.; Segalman, R. A.; Urban, J. J. Effect of Interfacial Properties on Polymer-Nanocrystal Thermoelectric Transport. *Adv. Mater.* **2013**, *25*, 1629−1633.
(65) Barako, M. T.; Roy-Panzer, S.; English, T. S.; Kodama, T.; Asheghi, M.; Kenny, T. W.; Goodson, K. E. Thermal Conduction in Vertically Aligned Copper Nanowire Arrays and Composites. *ACS Appl. Mater. Interfaces* **2015**, *7*, 19251−19259.
(66) Barako, M. T.; Sood, A.; Zhang, C.; Wang, J.; Kodama, T.; Asheghi, M.; Zheng, X.; Braun, P. V.; Goodson, K. E. Quasi-Ballistic Electronic Thermal Conduction in Metal Inverse Opals. *Nano Lett.* **2016**, *16*, 2754−2761.

https://doi.org/10.1021/acsaem.1c01420
ACS Appl. Energy Mater. 2021, 4, 8130−8141